Malaysian Journal of Chemistry, 2026, Vol. 28(2), 128-141

Gold as a Dopant to Enhance the Properties of $LiFePO_4$ Cathode Material for Lithium-Ion Battery Applications

Shahrul Izwan Ahmad[1], Fadhlina Che Ros[1], Fatin Nabilah Sazman[2], Mohamad Fariz Mohamad Taib[2], Muhd Zuazhan Yahya[3] and Fadhlul Wafi Badrudin[1],*
[1]Centre for Defence Foundation Studies, Universiti Pertahanan Nasional Malaysia,
57000 Kuala Lumpur, Malaysia
[2]Faculty of Applied Sciences, Universiti Teknologi MARA (UiTM), 40450, Shah Alam, Malaysia
[3]Faculty of Defence Science & Technology, Universiti Pertahanan Nasional Malaysia,
57000, Kuala Lumpur, Malaysia
*Corresponding author (e-mail: fadhlul@upnm.edu.my)

Improving the performance of $LiFePO_4$ cathode materials is critical for developing safer batteries and achieving high efficiency. Although their performance is hindered by low electronic conductivity, doping with transition metals can be used to enhance the structural, mechanical and electronic properties of $LiFePO_4$. In this work, the properties of gold-doped $LiFePO_4$ were investigated using first-principles calculations based on density functional theory (DFT), with the exchange–correlation effects treated by applying the Generalized Gradient Approximation (GGA) and the GGA+U method. Gold (Au) was selected as a dopant because of its unique electronic configuration, large atomic radius, chemical inertness and suitability for theoretical benchmarking. An iron (Fe) atom of $LiFePO_4$ was replaced with Au. Upon doping, the volume change between the delithiated and lithiated phases of Au-$LiFePO_4$ was reduced from 5.8 % to 1.7 % compared to $LiFePO_4$. The crystal system of Au-LFP exhibited mechanical stability and good ductility; however, its strength and stiffness were slightly lower than those of the undoped crystal. The band gap reduction from 3.8 eV to 2.19 eV indicated improved electrical conductivity. The open circuit voltage (OCV) increased from 3.7 V to 4.7 V. Further, the migration energy of lithium ions decreased from 0.783 eV to 0.378 eV, demonstrating enhanced ionic conductivity. All these desirable properties are expected to improve the overall performance of $LiFePO_4$.

Keywords: Au-$LiFePO_4$, cathode materials, lithium-ion battery, first principles study, mechanical and electronic properties

Received: October 2025; Accepted: December 2025

The first Li-based battery was introduced in 1970. It was later withdrawn from the market due to several problems, the most critical being the deposition of lithium metal dendrites, which caused short-circuiting during charging [1]. In 1991, the first commercial Li ion intercalation cell (using $LiCoO_2$ as the cathode and graphite as the anode) was produced and commercialized by Sony Corporation [2]. Despite successful commercialization, hazard management and regulatory safety evaluations have become the primary concerns among users [3].

Since the first report in 1997 by Goodenough et al., lithium iron phosphate ($LiFePO_4$) has gained much attention from scientists and industry players due to its good safety features compared to $LiCoO_2$ [4]. In addition, it became a favourable cathode due to its high theoretical energy density (170 mAh g^{-1}), suitable working voltage (3.5 V), good thermal stability, flat voltage plateau, abundant resources, low material cost, and nontoxic nature [3,5,6]. Currently, $LiFePO_4$ (LFP) is widely used as a cathode material for rechargeable lithium batteries, which are common in portable electronic devices and the automotive industry. Nevertheless, it possesses some drawbacks, such as low electronic conductivity ($>10^{-9}$ S cm^{-1}), low ionic diffusivity (10^{-11}–10^{-10} S cm^{-1}), poor performance at low temperatures, and low volumetric energy, that hamper its use in high rate Li-ion batteries [3]. Since the introduction of LFP in 2010, the demand for lithium-ion-based batteries has grown faster due to daily lifestyle changes as well as the green movement to reduce the carbon footprint by introducing electric vehicles to replace hydrocarbon fuel-based vehicles [7]. In 2021, the global market for Li-ion batteries was valued at USD 41.9B, whereas the US market was only valued at USD 8.5B. This trend is predicted to grow exponentially until 2030, when the technology is accepted by the rest of the world [8].

There are three general strategies to overcome the drawbacks of LFP: applying a conductive layer coating, doping (includes substitution doping, co-doping, interstitial doping, anti-site, or vacancy), and material downsizing. Doping has become a prominent method as it may enhance electron ion conductivity and improve structural integrity of LFP cathode materials at the crystal level [9]. This method can usually be classified into four types: 1) doping/co-doping, which replaces one native atom or more with foreign atoms; 2) vacancy, which removes a native atom from the crystal to create a vacant defect; 3) interstitial, which adds foreign atoms into the crystal to create point defects; and 4) anti-site, which involves the replacement of any two or more native atoms in the crystal [10]. There are many more aspects that may be taken into consideration, such as the type of atom used to dope (whether it is a metal, nonmetal, heteroatom, rare earth, or heavy element) [6, 11–17], doping position (doping at surface, subsurface, inside, as bulk or in coating material) and combinations of these [5, 18–22].

Doping with transition metal elements, especially on the Fe site, has drawn the attention of many researchers [12, 14, 15, 23]. Ajit Jena and B. R. K. Nanda performed the first major study on the effects of doping on LFP using several transition metals such as vanadium, chromium, manganese, cobalt, and nickel [14]. With the exclusion of Mn, they found that doping reduced the band gap (BG), irrespective of the nature of the dopant, due to the atomically localized nature of the Bloch *d* electrons in this family. The increase in valence electrons in the dopant also led to an increase in the open-circuit voltage, and the effect of the impurities on the Li-ion diffusivity was short-ranged [14]. In another study, Hyun S. L. et al. successfully synthesized Mn-doped LFP for a highly transparent thin film battery application. However, improvement in electronic properties only arose at Mn-doped concentrations of ~23 % and these properties worsened at higher concentrations, while the thickness-dependent optical spectra limited the thickness below 250 nm [12].

Yuan G. et al. have reported on the effects of ruthenium (Ru) doping of LFP, which may improve its specific capacity while retaining good cycle life. Ru doping was found to shorten the Li^+ ion diffusion distance, raise the Fermi energy, and narrow the BG [13]. Meanwhile, Sn doping was found to improve electronic performance by lowering the BG by ~ 0.2 eV, as reported by Lianxi H. and Guohua T. [20]. They found that Sn doping at the surface was favoured over subsurface or bulk doping due to the lower doping energy and surface energy, while the effects of doping appeared to be local such that subsurface doping resembled bulk doping. They concluded that the Sn dopant could modify BG and local charge transfer, therefore improving the electronic performance of the charging process without capacity loss [20]. In terms of stability, Hao L. et al. reported that LFP doped with vanadium (V) could provide a bigger and comparably stable structure to facilitate Li^+ diffusivity. On the other hand, V-doping is believed to reduce the BG of LFP and FP, thus helping to improve crystal conductivity [15].

Since the structural and electronic performance of LFP may be modified by doping, it would be interesting to study the effects of different metals on these cathode materials. In this work, we conduct a first-principles study based on density functional theory (DFT) calculations on gold-doped $LiFePO_4$ (Au-LFP) in the bulk condition. Au is a multivalent element with a unique electronic configuration ($5d^{10}$ $6s^1$) and is thus a good candidate for Fe ion substitution. This substitution could induce localized electronic polarization and lattice relaxation, potentially enhancing ionic transport and conductivity. As a nonreactive element, Au may also act as an inert stabilizer in the structure [24]. To the best of our knowledge, gold atoms have not yet been evaluated as a dopant in LFP. Although doping with gold seems uneconomical, the knowledge gained by this specific research could lead to unforeseen breakthroughs in battery technology in the future. Scientific research often involves exploring unconventional avenues. This unique test case may help scientists gain a deeper understanding of the limitations of the $LiFePO_4$ cathode material and the dopant itself which could be valuable information in the long run. In this work, we investigate the structural, mechanical and electronic properties of the cathode material, including stability, ductility, structure distortion, band gap, open circuit voltage, voltage profile, migration energy, and density of state. All these are discussed in detail in the following sections.

METHODOLOGY

The olivine structure of pure LFP with a space group *Pnma* was constructed based on X-ray diffraction (XRD) refinement data using Material Studio Visualizer [25]. To simulate doping conditions, one Fe atom was replaced with an Au atom in the $LiFePO_4$ unit cell with 28 atoms in four formula units, which resulted in a doped material with the chemical formula $LiFe_{0.75}Au_{0.25}PO_4$. Although most studies usually used lower concentration levels, this concentration was selected as it simulates a practical upper limit of dopant incorporation and is widely employed in first-principle studies of cathode materials [6, 26, 27]. All calculations were performed using generalized gradient approximation (GGA) with the Perdew-Burke-Ernzerhof (PBE) scheme [28] within the framework of density functional theory (DFT), as implemented in Cambridge Serial Total Energy Package (CASTEP) computer code [29]. The energy differences between the ferromagnetic (FM) and antiferromagnetic (AFM) configurations were very small; thus for simplicity, the FM configuration was assumed for the entire calculation [30,31]. The spin-polarized option was considered due to the presence of Fe. The cut-off energy of 700 eV was set together with a Monkhorst-Pack [18] k-point grid of 2 × 4 × 6 for the Brillouin Zone sampling after being evaluated through convergence tests.

The structure, was optimized using the Broyden-Fletcher-Goldfarb-Shanno (BFGS) algorithm until the self-consistent-field (SCF), reached the following convergence conditions: maximum energy change per atom of 5×10^{-6} eV, maximum force of 0.01 eV/Å, maximum stress of 0.02 GPa and maximum atom displacement of 0.0005 Å. Since LFP contained Fe ions, which are highly correlated, the usage of GGA-PBE alone tends to underestimate its electronic properties due to a self-interaction error. The GGA + U method was used to correct the error by adding the U parameter to the d orbital of the transition metal. Employing Dudarev's method [32], a widely accepted $U_{\text{eff}} = 4.5$ eV [33] was applied to Fe atoms. The incorporation of the U parameter exerted negligible effects on the Au ion, as it was not a strongly correlated material.

RESULTS AND DISCUSSION

Structural Properties

The Au-LFP crystal structure consists of four PO_4 tetrahedrons, three FeO_6 and one AuO_6 octahedrons with the lithium ions located in a one-dimensional channel along the z-axis as shown in Figure 1. Upon lithium extraction, Au-doped $FePO_4$ (Au-FP) retained the same crystal arrangement with minimal distortion. There were no major displacements or altered arrangements of atoms within the unit cell for both the lithiated and delithiated phases compared to undoped crystals. Thus Au doping did not significantly change the original structure, except the local environment around the Au atom [20].

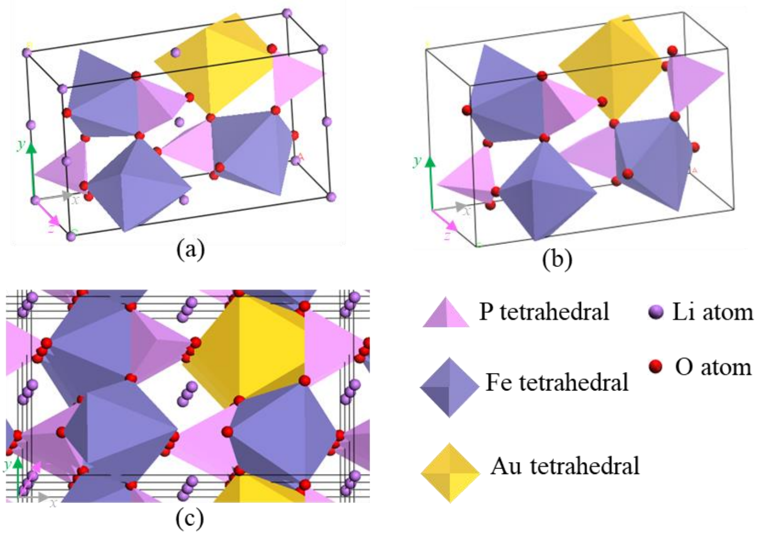

Figure 1. Crystal structures of (a) Au-LFP, (b) Au-FP, and (c) lithium ions located in a one-dimensional channel along the z-axis inside the crystal structure.

Table 1. The average calculated values for bond length (BL) in Å and bond order (BO) for Au-LFP, Au-FP, LFP, and FP.

Structure	Au-LFP		Au-FP		LFP		FP	
	BL	BO	BL	BO	BL	BO	BL	BO
P–O	1.5418	0.648	1.5340	0.6183	1.5410	0.6525	1.5350	0.6300
Fe_1–O	2.1505	0.2333	2.0910	0.235	2.1613	0.2133	2.0615	0.2433
Fe_2–O	2.1429	0.2367	2.0898	0.2300	2.1613	0.2133	2.0615	0.2433
Fe_3–O	2.1513	0.2350	2.0813	0.2400	2.1613	0.2133	2.0615	0.2433
Fe_4–O	-	-	-	-	2.1613	0.2133	2.0615	0.2433
Au–O	2.4602	0.0867	2.3495	0.2000	-	-	-	-
Li_1– O	2.2077	0.0767	-	-	2.1697	0.0800	-	-

Table 1 lists the average bond length (BL) and bond order (BO) values of the respective bonds obtained from the Mulliken analysis. The BO values ranged from 0 to 1 to indicate the character of the chemical bond from ionic to covalent [34]. In the case of the P-O bond in Au-LFP, the average BL and BO values showed no significant changes after lithium-ion removal, with a minuscule reduction in length and order. The values shown were also almost similar as compared to pristine LFP, which indicates the rigidness of the bond, suggesting that the structure of the cathode material was maintained. These also imply that Au doping was unlikely to induce phase changes in the crystal structure.

For the Fe-O bond in Au-LFP and Au-FP, the average BO values were slightly larger (~10 % more) than those of the undoped counterparts. These situations indicate stronger Fe-O bonding in the Au-LFP crystal, which is good as it prevents the dissociation of Fe ion into the electrolyte, while bonded O atoms prevent O_2 gas generation. This leads to improved electrochemical stability and enhanced safety features for cathodes in batteries [35]. Stronger Fe-O and P-O bonds give rise to a firmer and more rigid structure that enables a battery to endure harsh conditions and withstand repeated charge and discharge activities [36].

On the other hand, the average BL for Fe-O and Au-O reduced after lithium ion removal. This is due to the fact that the increase in BO was accompanied by a decrease in BL. However, some individual BLs showed an increase in length, e.g., the average length of two Au-O bonds increased significantly from 2.57 Å to 2.96 Å. Also, the angle between the Au-O bond was distorted, possibly due to the change of one of its BO values from 0.03 to –0.03 (indicating antibonding), where the two atoms prefer to move apart [37]. The introduction of a *d*-type cation in the crystal may induce stronger Coulomb repulsions between cations and electrons originating from ligands, generating internal stress and distortion [6]. As a result, the lattice parameters *b* and *c* increase, eventually enlarging the volume of the delithiatied phase.

To obtain a broader perspective, the volume changes between the lithiated and delithiated phases (Δ volume) of the respective cathode materials were assessed. A firmer structure with small changes in volume is crucial to prevent cracking, deformation, or crumbling of the electrode material [38] and interface degradation [1]. Volume changes for several cathode materials are shown in Table . The volume changes for pristine LFP determined by experiment and calculation were 6.8 % and 5.8 %, respectively, while Au-LFP had a significantly smaller value of 1.7 %. Almost no change was detected in the Fe-O bond order of Au-LFP compared to Au-FP. This phenomenon may be the reason for the smaller volume change. This indicates that doping LFP with gold may reduce volume and structure fluctuations during the charging-discharging process, resulting in better cycle performance and improving structural properties of cathode materials overall.

Mechanical Properties

Stability is a crucial factor influencing the electronic performance of battery cathode materials. If a material lacks stability, it is susceptible to phase changes and degradation, which can negatively impact the battery's charge and discharge capabilities. Hence, calculating the material's stability is essential. The elastic constant C_{ij} is a widely used parameter to describe the relationship between stress and strain in a material. Within the elastic limit and small strain conditions, C_{ij} may be employed to assess the mechanical stability of a material. In an orthotropic system, the elastic constants C_{11}, C_{22}, and C_{33} represent the material's linear compression moduli along the X, Y, and Z axes, respectively. Similarly, C_{44}, C_{55}, and C_{66} represent the shear moduli in the (100), (010), and (001) planes, while C_{12}, C_{13}, and C_{23} correspond to the longitudinal and transverse shrinkage.

Table 3 illustrates the elastic constants C_{ij} for undoped LFP and Au-LFP. The values for the LFP calculated in this study are aligned with those reported in a prior study [39]. According to the Born criterion, the mechanical stability of an orthotropic crystalline system should meet the following conditions [40]:

$$C_{11} > 0,\ C_{22} > 0,\ C_{33} > 0,\ C_{44} > 0,\ C_{55} > 0,\ C_{66} > 0,\ C_{11} + C_{22} + C_{33} + 2(C_{12} + C_{13} + C_{23}) > 0,\ (C_{11} + C_{22} - 2C_{12}) > 0,\ (C_{11} + C_{33} - 2C_{13}) > 0,\ (C_{22} + C_{33} - C_{23}) > 0 \quad (1)$$

Table 2. Comparison of lattice constants between lithiated and delithiated phases of LFP structures.

Structure	a(Å)	b(Å)	c(Å)	Volume (Å^3)	Δ Volume	Ref
$LiFePO_4$ (Exp.)	10.332	6.010	4.692	291.351	6.8%	[33]
$FePO_4$ (Exp.)	9.810	5.790	4.780	271.504		[34]
$LiFePO_4$ (DFT)	10.351	6.024	4.722	294.338	5.8%	[26]
$FePO_4$ (DFT)	9.773	5.886	4.821	277.323		[26]
Au-$LiFePO_4$ (DFT)	10.630	6.083	4.789	309.654	1.7%	This work
Au-$FePO_4$ (DFT)	10.157	6.207	4.996	314.862		This work

Table 3. Elastic constants (in GPa) for pristine LFP and Au-LFP.

	C_{11}	C_{22}	C_{33}	C_{44}	C_{55}	C_{66}	C_{12}	C_{13}	C_{23}
LFP [41]	148.80	190.10	179.20	39.00	53.30	50.00	74.90	56.60	46.30
LFP calc.	139.05	186.16	170.91	38.32	44.11	38.01	67.59	57.75	48.22
Au-LFP calc.	119.22	150.78	152.12	23.46	28.60	32.00	74.07	51.92	47.85

Using the elastic constants listed in Table 3, both undoped and doped LFP were found to meet the mechanical stability conditions. This implies that the doping process did not compromise the material's mechanical stability, indicating the mechanical feasibility of doping. After obtaining the elastic constants for both doped and undoped materials, two common methods are used to calculate their bulk and shear moduli. The Voigt method assumes uniform strain in all grains, while the Reuss method assumes uniform stress. These approaches provide the upper and lower limits of polycrystalline material constants, and their averages can be used as more accurate estimates of bulk and shear moduli. The expression of bulk modulus, *B* and shear modulus, *G* can be determined based on the average value as in the following equations:

$$G = \frac{G_V + G_R}{2} \quad (2)$$

$$B = \frac{B_V + B_R}{2} \quad (3)$$

where G_V and G_R are the shear moduli, and B_V and B_R are the bulk moduli obtained using the Voigt and Reuss methods. Next, the Young's modulus, *E* and Poisson's ratio, *v* can be calculated using the following equations [42]:

$$E = \frac{9BG}{3B+G} \quad (4)$$

$$v = \frac{3B-2G}{6B+2G} \quad (5)$$

The physical properties of undoped LFP and Au-doped LFP, including bulk modulus, shear modulus, Young's modulus, Poisson's ratio, and *B/G* ratio, were calculated and listed in Table 4, together with the results of some other dopants for comparison. For materials, the bulk modulus quantifies resistance to radial compressive strain, while the shear modulus measures resistance to shear strain, with larger values indicating greater stiffness. Young's modulus describes the material's tendency to deform under pressure, reflecting resistance to deformation.

From Table 4, it can be seen that the mechanical properties of LFP, in terms of *B*, *G*, and *E*, decreased after doping with Au, indicating a slight reduction in strength and stiffness caused by the lower Au-O bond order. However, Poisson's ratio, *v*, which describes the material's deformation under compression or tension, decreased slightly in the doped material, suggesting that it was less likely to deform under shear stress compared to the undoped version. Ductility significantly impacts the cycling and performance of lithium-ion batteries. To evaluate ductility and brittleness, the Pugh criterion was applied, using the *B/G* value. A *B/G* value greater than 1.75 indicates good ductility, while lower values suggest brittle behaviour. The *B/G* values of LFP before and after doping were 2.09 and 1.99, respectively, both indicating good ductility.

Table 4. The Bulk modulus (*B*, in GPa), Shear modulus (*G*, in GPa), Young's modulus (*E*, in GPa), Poisson's ratio (*v*) and *B/G* ratio values for pristine LFP and doped-LFP.

	B	*G*	*E*	*v*	*B/G*
LFP [41]	-	-	1238.30	0.28	1.93
LFP calc.	93.28	44.68	115.59	0.29	2.09
Au-LFP calc.	76.77	38.65	99.28	0.28	1.99
Co-LFP [43]	143.2	51	136.7	0.3	1.9
N,Nb-LFP [41]	95.0	54.1	136.3	0.26	1.76

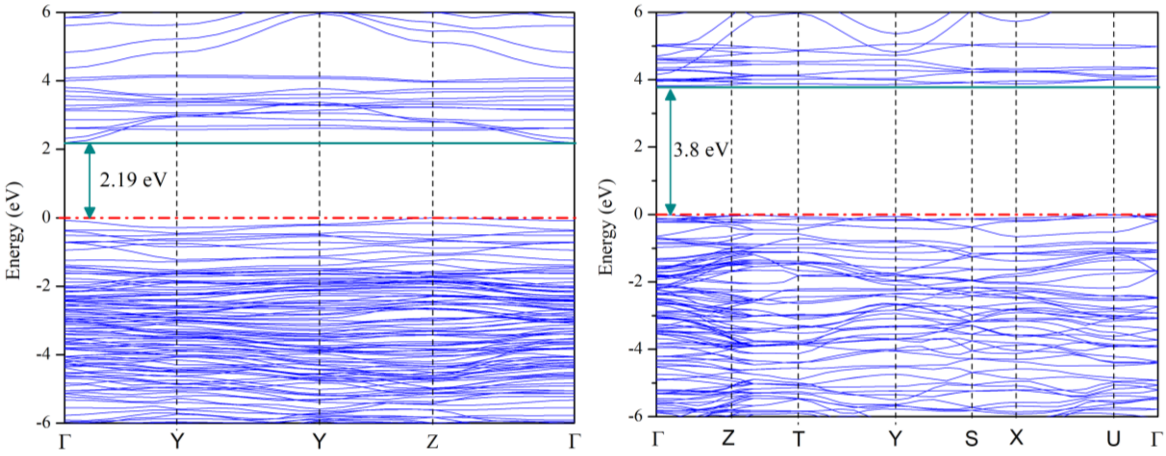

Figure 2. Band structures for (a) Au-LFP and (b) pristine LFP.

Band Gap Determination

The most important characteristic of a battery is its electronic conductivity, which is always associated with the band gap. A cathode material with a small band gap requires less energy to excite electrons from the valence band to the conduction band compared to a material with a larger band gap. Using the DFT technique, the density of state of the electrons can be extensively calculated and projected as a graph against energy. Physical properties such the lattice constant, bond length, bond order, and magnetic properties of bulk materials that contain transition metals are accurately predicted by various functionals such as GGA and LDA. However, the well-established LDA and GGA functionals normally encounter issues when calculating band gaps for semiconductors, insulators, and strongly correlated systems, which some refer to as "the band gap problem" [44]. These functional underestimate the exchange interaction among the strongly localized electrons of partially filled 3*d* orbitals in materials such as transition metals or rare earth compounds. This causes underestimation of the stability of high-spin states in impurity centres or ligand fields, which leads to the prediction of ground states with incorrect spin multiplicities.

To address this issue, the Hubbard U correction was applied, resulting in the so-called LDA + U or GGA + U approaches. Without these approaches, wrong interpretations of electronic structures may be obtained, e.g., where the LFP would have a metallic, instead of an insulating character. Hubbard U is a parameter that adds terms to the typical DFT Hamiltonian, such as GGA and LDA functionals, to account for the on-site Coulomb repulsions between electrons in partially filled *d* or *f* orbitals, in this case, Fe atoms. Au atoms, however, are not affected by this problem and the addition of the U parameter on Au atoms does not have a significant effect. Therefore, the electron potential within the transition metal or rare earth atom radii was modified from the GGA by an amount proportional to the U parameter given. Since the GGA + U method has little additional computational cost, it has become a recognized way to study transition metal compounds. Previously, we successfully determined the best U value for the Fe atom as 4.5 eV when investigating the electronic properties of LFP cathode materials [33].

The calculated values of the band gaps for Au-LFP compared to LFP using the GGA+U approach were 2.19 eV and 3.8 eV respectively, as shown in Figure 2. While the delithiated phase of Au-FP and FP are 0.86 eV and 1.5 eV respectively. These values proved that Au doping significantly reduced the band gap. The smaller band gap makes electron migration from the valence band to the conduction band easier, implying better electronic conductivity. The orbital electronics and states will be discussed further in the partial density of state (PDOS) section.

Open Circuit Voltage

The open circuit voltage, also known as OCV, is an important parameter that can be used to characterize the size of the driving forces of the electrical charges between the cathode and anode, once they are connected [45]. Increasing the OCV value is one of the easier ways to achieve a high specific energy battery (according to the formula, energy = capacity × voltage) compared to developing a new cathode material with higher specific capacity [46]. Since electrons move between the cathode and anode through an external circuit along with lithium in the electrolyte during charging and discharging, the OCV of a Li-ion battery can be interpreted from the perspective of the Gibbs free energy [47]. Disregarding volume and entropy effects, it has been generally accepted that the average voltage for lithium insertion/extraction from a material is given by

$$V_{\mathrm{ocv}} = -\frac{G\left[\mathrm{Li}_{x_2}\mathrm{Host}\right] - G\left[\mathrm{Li}_{x_1}\mathrm{Host}\right] - (x_2 - x_1)G[\mathrm{Li}]}{x_2 - x_1} \tag{6}$$

where G is the Gibbs free energy of the material. $x_1 = 0$ and $x_2 = 1$ are usually considered the limits of the lithiated and delithiated phases [44]. Typically, the free energies can be replaced by the ground state energies with very little error [48]. Hence, the energies of Au-LFP, Au-FP, and lithium metal were calculated to determine the voltage for lithium intercalation.

The OCV value for Au-LFP was calculated to be 4.7 V. This OCV value appears to be large compared to that of pristine LFP and other cathode materials, especially $LiCoO_2$ (4.1 V). A comparison of the OCV values of different types of cathode materials are shown in Table 5. Higher OCV values would be beneficial for high-power applications that require higher voltage batteries, such as EVs and HEVs. However, for a practical cathode material, the OCV should be optimal to store the maximum amount of energy in the cell and, concurrently, prevent decomposition of the electrolyte due to high voltage [14]. Reassuringly, there is ongoing research focussing on improving and developing electrolytes for high voltage batteries [49,50].

The voltage profiles of Au-LFP and LFP at various Li concentrations was generated, as shown in Figure 3. The voltage profiles were calculated under the assumption of equilibrium conditions. With the decreased concentration of lithium ions (stepwise from 1, 0.75, 0.5, 0.25 until 0), the voltage of both LFPs also decreased stepwise, creating a multiple plateau in the voltage profile. The same trend indicated the same charging-discharging properties, with the only difference being the initial OCV. Similar observations have been reported by many researchers [54–57]. The voltage values were approximately similar for the same number of lithium atom absences, while voltage drop among phases were almost the same. This property suggests stable intermediate phases [54], which is a good characteristic for battery applications.

Table 5. OCV values of several cathode materials.

Materials	Method	OCV	Reference
$LiMnPO_4$	Experimental	4.1 V	[48]
$LiNiO_2$	Experimental	3.85 V	[51]
$LiCoO_2$	Experimental	4.1 V	[52]
$LiFePO_4$	Experimental	3.5 V	[53]
$LiFePO_4$	GGA-PBE + U	3.45 V	[33]
Au-$LiFePO_4$	GGA-PBE + U	4.7 V	This work
Au-$LiFePO_4$	GGA-PBE (without U)	4.2 V	This work

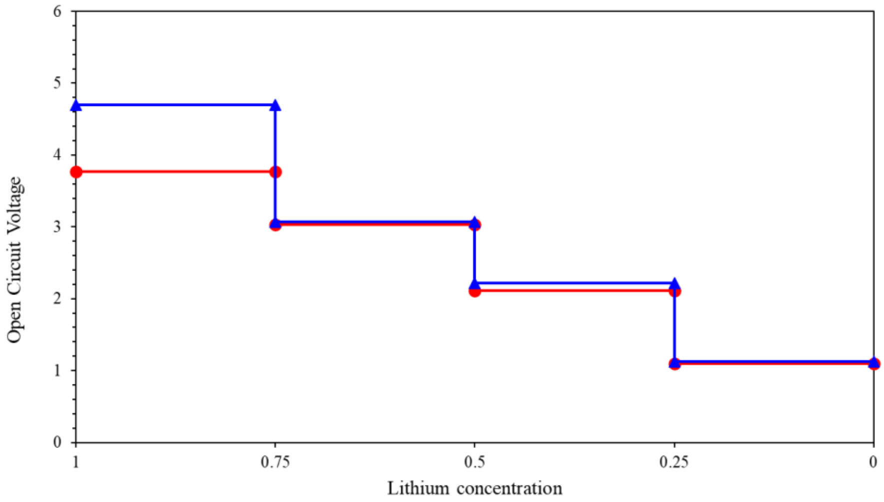

Figure 3. Voltage profiles for Au-LFP (blue line) and LFP (red line).

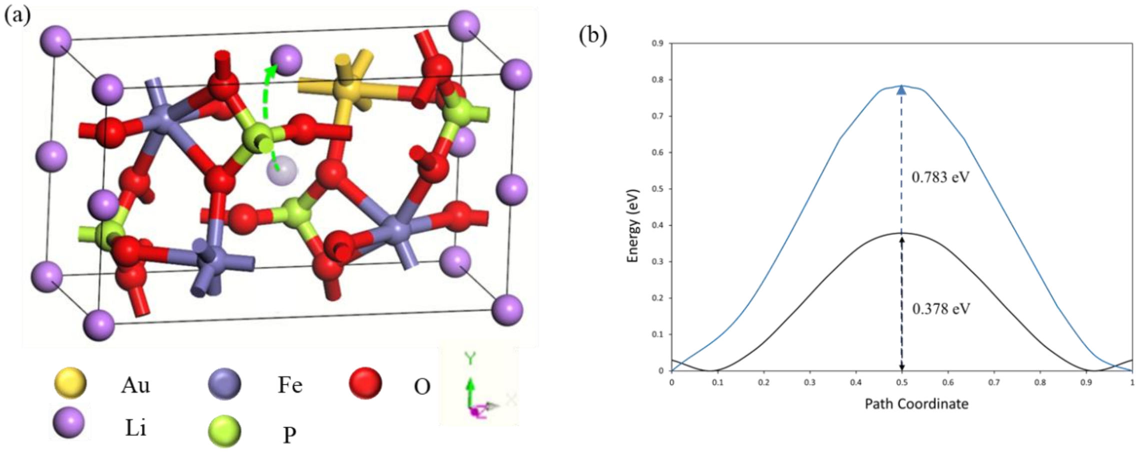

Figure 4. (a) Mechanism of lithium-ion diffusion through the cell in [010] direction and (b) Nudge elastic band result for the migration energy of lithium ion diffusion along the respective path for pristine LFP (blue) and Au-LFP (black).

Table 6. Calculated and experimental values for the migration energy of cathode materials.

Materials	Method	Migration Energy	References
$LiFePO_4$	Calculation using GULP code	0.55 eV	[54]
$LiFePO_4$	Determine from the experimental sample	0.563 eV	[55]
$LiFePO_4$	Calculation using CASTEP code	0.838 eV	[56]
$LiFePO_4$	Calculation using CASTEP code	0.783 eV	Our work
Au- $LiFePO_4$	Calculation using CASTEP code	0.378 eV	Our work

Migration Energy

The ability of a cathode to easily allow lithium ions to diffuse determines the performance of the electrode, and this depends on the diffusion migration energy of the cathode material. A low diffusion barrier and high lithium ion mobility are highly desirable. We examined the migration path of lithium ions and estimated the migration energy base with the Nudged Elastic Band (NEB) method by applying a complete linear and quadratic synchronous transit (LST/QST) protocol in determining the transition state (TS) search algorithm in CASTEP.

We only considered the lithium migration pathway along the [010] direction as it resulted in a notably low migration energy compared to other pathways. This pathway is desirable as it created a 1-dimensional (1-D) channel that allowed the lithium ions to drift with the least resistance [58]. The lithium ion travelled through the channel almost in a straight line from the centre to the edge of the cell with a very small bend in the middle of the path, as shown in Figure 4(a). This indicates that ions may have flowed easily through the channel with less distortion from the atom potential inside the cell itself, thus suggesting better ion conductivity.

To ensure accuracy, the migration pathway was examined using 5–15 intermediate images before the converged migration energy was determined. The result from NEB analysis for undoped LFP was compared to other results. This was to validate the calculated value using this method for Au-LFP. The calculated value of the migration energy for undoped LFP was 0.783 eV which is in agreement with another study, as summarized in Table 6. Figure 4 (b) shows the energy level of a lithium ion against the path coordinate. The migration energy, calculated from the lowest to the highest energy level (also known as the saddle point), was 0.378 eV. This diffusion barrier showed significant improvement when compared to the calculated value of undoped LFP, which was 0.783 eV. As mentioned in the previous section, the presence of an Au atom enlarged the size of the unit crystal, creating more space for the lithium ion to flow through the crystal structure along the [010] direction. This condition results in better ionic conductivity of the lithium ion and increases its capability to be used in high charge-discharge rate batteries [59]. However, such a 1-D channel is anisotropic and prone to be affected by blockage and distortion [60].

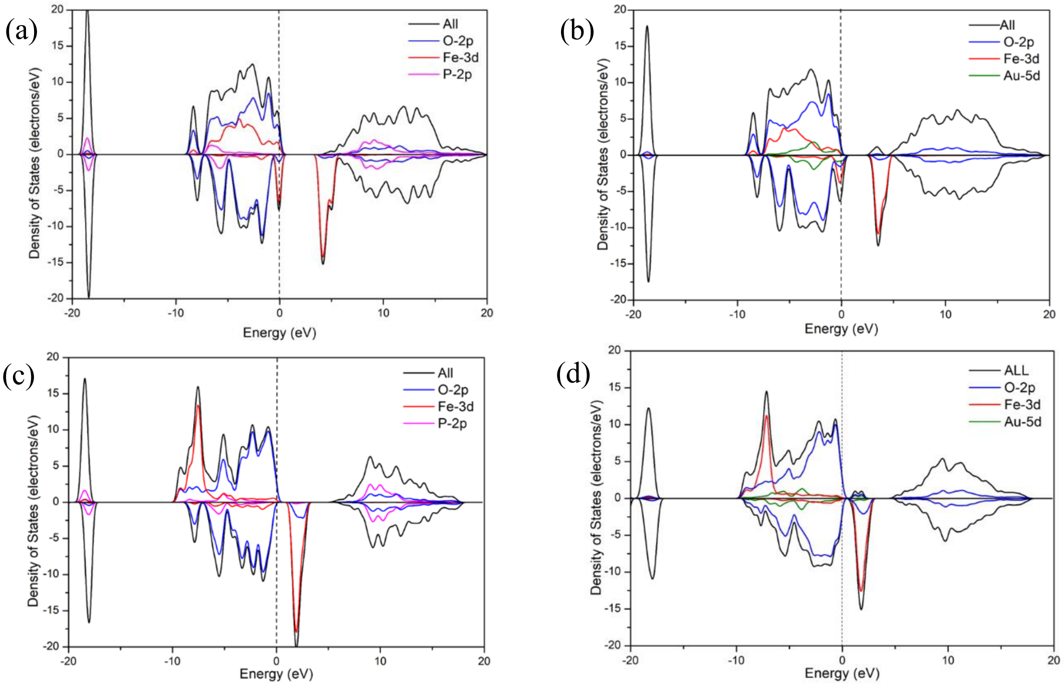

Figure 5. PDOS of respective elements in (a) LFP, (b) Au-LFP, (c) FP and (d) Au-FP.

Partial Densities of States

It is well known that most doped LFP materials exhibit enhanced electronic performance compared to pure olivine LFP [14]. This is due to the band gap reduction, which directly reduces the resistivity of the cathode material, thus improving electronic conductivity. The origin of such an improvement cannot be clearly grasped through experimental analysis. Nevertheless, the band gap reduction can be understood by comparing the partial densities of states (PDOS) of the doped compounds and the corresponding pristine compounds [14].

To gain insight into the electronic states of the *s*, *p*, and *d* orbitals, the partial densities of states (PDOS) graphs for the lithiated and delithiated Au-LFP cathode materials are presented in Figure 5. On the energy axis, the Fermi level was set at 0 eV, in which the valence band is located below the Fermi level, and the conduction band is located above the Fermi level [61]. All data were obtained using GGA-PBE + U, with a U value for Fe of 4.5 eV. The DOS shapes for LFP and FP obtained in this study were identical to those in other reports [62,63], while the calculated band gaps for pristine LFP and FP were 3.822 eV and 1.505 eV respectively, in good agreement with previously reported values [20,64]. This is a good basis to further investigate the PDOS of Au-doped LFP.

In Figure 5, the main contribution to the maximum valence band (MVB) of all samples was from the O 2*p* and Fe 3*d* states. A much smaller Au 3*d* state contribution was observed in the case of gold-doped samples, due to its small number of samples. On the other hand, the contribution of the 2*p* bands of P in the valence band was insignificant. Meanwhile, the minimum conduction band (MCB) in all samples was mostly dominated by the Fe 3*d* state with small contributions from the O 2*p* and Au 6*s* states. By comparing the respective lithiated and delithiated phases, the contribution of the spin-down Fe 3*d* state in the VBM vanished due to the loss of one 3*d* electron, clearly indicating a transition from Fe^{2+} to Fe^{3+}.

Introducing a gold atom into the crystal showed that the Au 5*d* state resided in MVB, mostly near the Fermi level. Interestingly, upon doping, the CBM of Fe shifted closer to the Fermi level, which was most likely influenced by the presence of the gold atom. This resulted in a narrower gap between CBM and VBM, which contributes to increased electronic conductivity [15]. Such observation was also reported by Rosseinsky et al., who suggested that the change in band gap was attributed to cation lattice interactions [65]. On the other hand, Wojdel and Bromley described a decrease in band gap values when intercalation with an ionic atom caused a lattice expansion effect [66], which is consistent with our results.

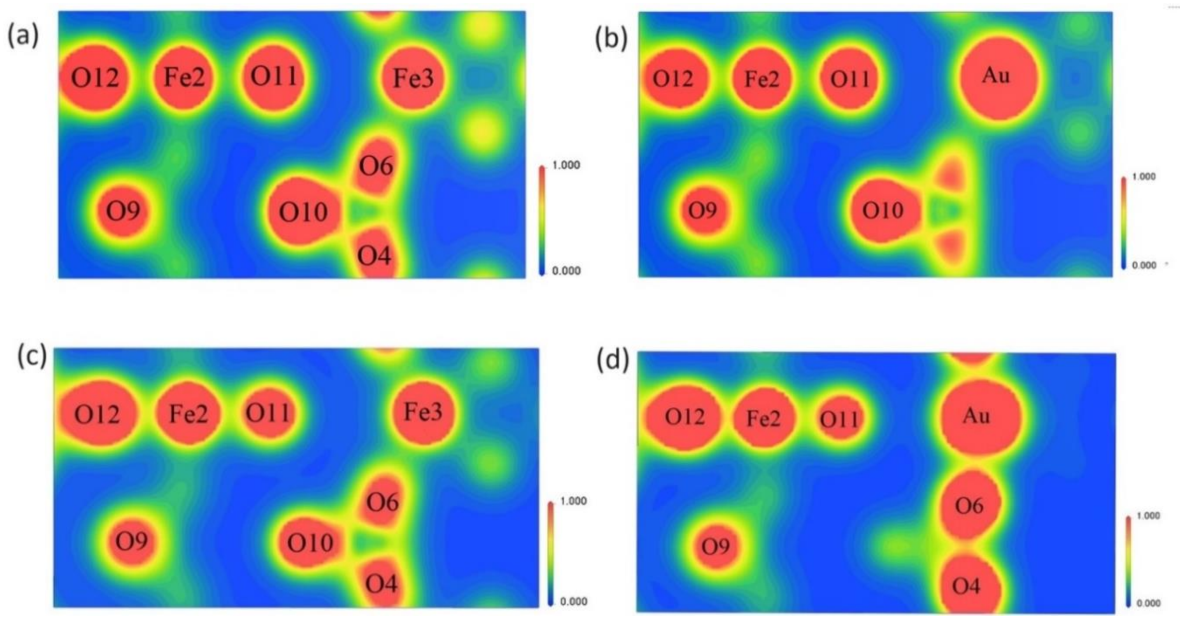

Figure 6. Electron density map for (a) LFP, (b) Au-LFP, (c) FP, and (d) Au-LFP.

Electron Density Mapping

To further examine the chemical nature and electron distribution of the doped materials, we plotted the electron density-difference maps with a range of field density as visualized in Figure 6. The scale of electron density represented in Figure 6 ranged from 0 e/Å^3 (blue), which indicates the lowest probability of electron density, to 1 e/Å^3 (red), which indicates the highest probability of electron density.

The electron density of the Au atom (a round red shape) was slightly bigger in size, implying a higher density of electrons compared to the Fe and O atoms. The bonding between Au and O4 became more obvious as the cloud of electrons came closer in the delithiated phase, as shown Figure 6(d). The bond order of Au-O4, rising from 0.17 in the lithiathed phase to 0.26 in the delithiated phase. The same phenomenon was observed for Fe2, O11, and O12, where the average bond order increased from 0.27 (lithiated) to 0.35 (delithiated). Such a condition indicates stronger covalent bonding, which results in a rigid structure that is chemically resistant to electrolytic corrosion. The blue region of Au-FP in Figure 6 (d), which indicates a high probability of electron absence, seemed larger compared to that of undoped FP. This may facilitate the mobility of lithium ions, thus increasing the ionic conductivity of cathode material. Therefore, the effect of gold doping could improve the structural and electronic properties of LFP cathode materials.

CONCLUSION

Structural, mechanical, electronic and electrochemical studies on Au-doped LFP were conducted by first principles, based on density functional theory. The crystal structure of Au-doped LFP was slightly larger as the Au ion had a larger ionic radius compared to the Fe ion, which it replaced. This may enhance the Li-ion diffusivity in cathode materials. The insignificant changes in volume between the lithiated and delithiated phases of Au-LFP suggests that the structure was likely to maintain its structural stability, resulting in better structure retention during the charging and discharging process. The crystal system of Au-LFP exhibited mechanical stability and good ductility, however its strength and stiffness were slightly lower than those of the undoped crystal. From the Mulliken analysis, a stronger Fe-O bond was observed in the Au-LFP and Au-FP crystal; this may prevent the dissociation of Fe ions into the electrolyte and create strongly bonded O atoms to prevent O_2 gas generation. This is an important durability and safety feature for a battery cathode. Furthermore, the introduction of a *d*-type cation in the crystal may cause stronger Coulomb repulsion between cations and electrons, resulting in internal stress and distortion, thus explaining the volume enlargement of the delithiatied phase. The presence of a gold atom affected the conduction band of Fe by shifting it closer to the Fermi level, thus reducing the Au-LFP band gap and improving electronic conductivity. At the same time, migration energy also decreased, a direct indication of better ionic conductivity. The OCV of the Au-doped LFP also increased. However, alternative electrolytes and a better battery management system are needed to support this new environment. Overall, this study proved that doping with gold atoms improved the structural and electronic properties of LFP in many aspects. It offers strong potential for high-power batteries and their use in rugged conditions, despite making it suitable for theoretical benchmarking for further exploration.

ACKNOWLEDGEMENT

This work was supported by an internal UPNM grant (Grant code: UPNM/2021/GPJP/STG/2). The authors would like to express their gratitude to the Core Group for Academic Development and Research Experts (CADRE), in the Centre for Defence Foundation Studies, Universiti Pertahanan Nasional Malaysia, and the Institute of Science, Universiti Teknologi MARA (UiTM) for their support in providing the facilities to carry out this research.

REFERENCES

1. Zhang, Y., Zuo, T. -T., Popovic, J., Lim, K., Yin, Y. -X., Maier, J., et al. (2020) Towards better Li metal anodes: Challenges and strategies. *Materials Today*, **33(March)**, 56–74.

2. Satyavani, T. V. S. L., Srinivas Kumar, A. and Subba Rao, P. S. V. (2016) Methods of synthesis and performance improvement of lithium iron phosphate for high rate Li-ion batteries: A review. *Engineering Science and Technology, an International Journal*, **19(1)**, 178–188.

3. Hu, J., Huang, W., Yang, L. and Pan, F. (2020) Structure and performance of the LiFePO4cathode material: From the bulk to the surface. *Nanoscale*, **12(28)**, 15036–15044.

4. Padhi, A. K., Nanjundaswamy, K. S. and Goodenough, J. B. (1997) Phospho-olivines as Positive-Electrode Materials for Rechargeable Lithium Batteries. *Journal of The Electrochemical Society*, **144(4)**, 1188–1194.

5. Xu, G., Zhong, K., Zhang, J. M. and Huang, Z. (2014) First-principles investigation of the electronic and Li-ion diffusion properties of LiFePO4 by sulfur surface modification. *Journal of Applied Physics*, **116(6)**, 1–7.

6. Molenda, J., Kulka, A., Milewska, A., Zajac, W. and Świerczek, K. (2013) Structural, transport and electrochemical properties of liFePO4 substituted in lithium and iron sublattices (Al, Zr, W, Mn, Co and Ni). *Materials*, **6(5)**, 1656–1687.

7. McKerracher, C., O'Donovan, A., Soulopoulos, N., Grant, A., Mi, S., Doherty, D., et al. (2022) *Electric Vehicle Outlook 2022*. Bloomberg Finance L.P. <https://about.bnef.com/electric-vehicle-outlook/> Accessed 25.08.25.

8. Grand View Research (2021) *Lithium-ion Battery Market Size, Share & Trends Analysis Report Forecasts, 2022 - 2030*. Grand View Research In. <https://www.grandviewresearch.com/industry-analysis/lithium-ion-battery-market> Accessed 25.08.25.

9. Yan, W., Yang, S., Huang, Y., Yang, Y. and Guohui Yuan (2020) A review on doping/coating of nickel-rich cathode materials for lithium-ion batteries. *Journal of Alloys and Compounds*, **819**, 153048.

10. Kuganathan, N., Srikaran, R., Fossati, P. C. M. and Chroneos, A. (2019) Theoretical modeling of defects, dopants, and diffusion in the mineral ilmenite. *Minerals*, **9(10)**, 1–13.

11. Liu, Z., Huang, X. and Wang, D. (2008) First-principle investigations of N doping in LiFePO4. *Solid State Communications*, **147(11–12)**, 505–509.

12. Lee, H. S., Kim, S., Parmar, N. S., Song, J. H., Chung, K. Yoon, Kim, K. B., et al. (2019) Carbon-free Mn-doped LiFePO4 cathode for highly transparent thin-film batteries. *Journal of Power Sources*, **434(May)**, 226713.

13. Gao, Y., Xiong, K., Zhang, H. and Zhu, B. (2021) Effect of Ru Doping on the Properties of LiFePO4/C Cathode Materials for Lithium-Ion Batteries. *ACS Omega*, **6(22)**, 14122–14129.

14. Jena, A. and Nanda, B. R. K. (2017) Engineering Diffusivity and Operating Voltage in Lithium Iron Phosphate through Transition-Metal Doping. *Physical Review Applied*, **7(3)**, 1–8.

15. Lin, H., Wen, Y., Zhang, C., Zhang, L., Huang, Y., Shan, B., et al. (2012) A GGAU study of lithium diffusion in vanadium doped LiFePO 4. *Solid State Communications*, **152(12)**, 999–1003.

16. Wang, Z., Zhao, C., Niu, X., Cheng, Y., Wang, L. and Huang, P. (2025) Titanium-doped α-Ni(OH)2 as a cathode material for high-performance nickel-metal hydride batteries. *Ionics*, **31(11)**, 11835–11841.

17. Kashyap, S. J., Gowthami, C., Purohit, S., Gautam, G. S., Srikanth, V. V. S. S., Vijay, R., et al. (2025) Synergistic effect on electro-chemical performance of LiFePO4 cathodes via carbon coating and Ni2+ doping: a combined experimental and theoretical approach. *Journal of Electroanalytical Chemistry*, **996(June)**, 119423.

18. Xu, G., Zhong, K., Zhang, J. M. and Huang, Z. (2015) First-principles study of structural, electronic, and Li-ion diffusion properties of N-doped LiFePO4 (010) surface. *Solid State*

Ionics, **281**, 1–5.

19. Timoshevskii, V., Feng, Z., Bevan, K. H. and Zaghib, K. (2015) Emergence of Metallic Properties at LiFePO4 Surfaces and LiFePO4/ Li2S Interfaces: An Ab Initio Study. *ACS Applied Materials and Interfaces*, **7(33)**, 18362–18368.

20. Hou, L. and Tao, G. (2017) A first-principles study of bulk and surface Sn-doped LiFePO4: The role of intermediate valence component in the multivalent doping. *Physica Status Solidi (B) Basic Research*, **254(10)**.

21. Zilong, Y., Dachuan, T., Jian, L. and Zhongming, N. (2021) First-principles insights into selenium and sulfur doping on Ti2CO2 MXene for mitigating the shuttle effect in lithium-sulfur batteries. *Chinese Physics C*, **45**, 124107.

22. To Van, N., Duy, N. V. A., Hieu, N. H., Ngo, Q. Q., Son Luong, T., Ngo, T. L., et al. (2025) Co-doping aluminum and boron enhances the stability and electrochemical properties of nickel-rich cathode materials for lithium-ion batteries. *Dalton Transactions*, **54(37)**, 14173–14190.

23. Liu, R., Guo, N., Luo, G. and Huang, Z. (2025) Synthesis and electrochemical performance of Zn2+-doped LiFePO4: towards high-rate and stable cathode materials for lithium-ion batteries. *Ionics*, **31(10)**, 10223–10230.

24. Wang, W., Meng, J., Yue, X., Wang, Q., Wang, X., Zhou, Y., et al. (2018) Synthesis and electrochemical properties of Li1.3Nb0.3Cr0. 4O2 as a high-capacity cathode material for rechargeable lithium batteries. *Chemical Communications*, **54(98)**, 13809–13812.

25. Streltsov, V. A., Belokoneva, E. L., Tsirelson, V. G. and Hansen, N. K. (1993) Multipole analysis of the electron density in triphylite, LiFePO 4, using X-ray diffraction data. *Acta Crystallographica Section B Structural Science*, **49(2)**, 147–153.

26. Lama, B., Smirnova, A. L. and Paudel, T. R. (2023) Enhanced Li-Ion Diffusivity of LiFePO4 by Ru Doping: Ab Initio and Machine Learning Force Field Results. *ACS Applied Energy Materials*, **6(20)**, 10424–10431.

27. Huang, Y., Liu, X., Yu, R., Cao, S., Pei, Y., Luo, Z., et al. (2019) Tellurium Surface Doping to Enhance the Structural Stability and Electrochemical Performance of Layered Ni-Rich Cathodes. *ACS Applied Materials and Interfaces*, **11(43)**, 40022–40033.

28. Perdew, J. P., Burke, K. and Ernzerhof, M. (1996) Generalized gradient approximation made simple. *Physical Review Letters*, **77(18)**, 3865–3868.

29. Clark, S. J., Segall, M. D., Pickard, C. J., Hasnip, P. J., Probert, M. I. J., Refson, K., et al. (2005) First principles methods using CASTEP. *Zeitschrift fur Kristallographie*, **220(5–6)**, 567–570.

30. Zhu, B., Lu, Z., Pickard, C. J. and Scanlon, D. O. (2021) Accelerating cathode material discovery through ab initio random structure searching. *APL Materials*, **9(12)**, 1–12.

31. Lu, Y., Li, J., Zhao, Y. and Zhu, X. (2019) Lithium Clustering during the Lithiation/ Delithiation Process in LiFePO4 Olivine-Structured Materials. *ACS Omega*, **4(24)**, 20612–20617.

32. Dudarev, S., Botton, G., Savrasov, S. Y., Humphreys, C. J. and Sutton, A. P. (1998) Electron-energy-loss spectra and the structural stability of nickel oxide: An LSDA+U study. *Physical Review B - Condensed Matter and Materials Physics*, **57(3)**, 1505–1509.

33. Ahmad, S. I., Badrudin, F. W., Abdullah, A. L. A., Yahya, M. Z. A., Taib, M. F. M. and Hassan, O. H. (2022) Evaluation of Olivine $LiFePO_4$ Polyanionic Cathode Material Using Density Functional Theory. *Key Engineering Materials*, **908**, 293–298.

34. Sazman, F. N., Nasir, N. A., Badrudin, F. W. and Ahmad, S. I. (2020) Effect of Water Molecules Toward the Structural and Electronic Properties of Prussian Blue Cathode Material for Potassium Battery: A First Principles Investigation. *International Journal of Nanoelectronics and Materials*, **13**, 75–82.

35. Wang, J. and Sun, X. (2012) Understanding and recent development of carbon coating on LiFePO 4 cathode materials for lithium-ion batteries. *Energy and Environmental Science*, **5(1)**, 5163–5185.

36. Mohamad Firdaus, R., Fadhlul Wafi, B., Siti Munirah, H., Siti Aminah, M. N., Mohamad Fariz, M. T. and Muhd Zu Azhan, Y. (2020) Benefits of Molybdenum Substitution in Na3V2(PO4)3 Cathode Material for Sodium Ion Batteries: A First Principles Study. *International Journal of Nanoelectronics and Materials*, **13**, 235–242.

37. Shang, S. L., Wang, Y., Mei, Z. G., Hui, X. D. and Liu, Z. K. (2012) Lattice dynamics, thermodynamics, and bonding strength of lithium-ion battery materials LiMPO 4 (M = Mn, Fe, Co, and Ni): A comparative first-principles study. *Journal of Materials Chemistry*, **22(3)**, 1142–1149.

38. Wang, X., Cao, X., Bourgeois, L., Guan, H., Chen, S., Zhong, Y., et al. (2012) N-doped graphene-SnO 2 sandwich paper for high-performance lithium-ion batteries. *Advanced Functional Materials*, **22(13)**, 2682–2690.

39. Banerjee, A., Araujo, R. B. and Ahuja, R. (2016) Unveiling the thermodynamic and kinetic properties of NaxFe(SO4)2 (x = 0-2): toward a high-capacity and low-cost cathode material. *Journal of Materials Chemistry A*, **4(46)**, 17960–17969.

40. Wu, Z., Hao, X., Liu, X. and Meng, J. (2007) Structures and elastic properties of Os N2 investigated via first-principles density functional calculations. *Physical Review B - Condensed Matter and Materials Physics*, **75(5)**, 1–6.

41. Chen, J., Wang, F., Yin, M. and Yao, C. (2022) First-Principles Study on the Electronic Properties and Mechanical Stabilities of Anion-Cation Multiple-Doped LiFePO4. *ChemistrySelect*, **7(38)**, 1–7.

42. Caravaca, M. A., Miño, J. C., Pérez, V. J., Casali, R. A. and Ponce, C. A. (2009) Ab initio study of the elastic properties of single and polycrystal TiO 2, ZrO 2 and HfO 2 in the cotunnite structure. *Journal of Physics: Condensed Matter*, **21(1)**, 015501.

43. Lv, Z., Li, M., Yang, H., Lin, J., Luo, J., Hong, R., et al. (2024) The first-principles study on electrochemical performance, mechanical properties, and lithium-ion migration of LiFePO4 modified by doping with Co and Nb. *Journal of Solid State Electrochemistry*, **28(8)**, 2873–2883.

44. Zhang, Y., Alarco, J. A., Best, A. S., Snook, G. A., Talbot, P. C. and Nerkar, J. Y. (2019) Re-evaluation of experimental measurements for the validation of electronic band structure calculations for LiFePO 4 and FePO 4. *RSC Advances*, **9(2)**, 1134–1146.

45. Shi, J., Wang, Z. and Fu, Y. Q. (2016) Density functional theory study of diffusion of lithium in Li–Sn alloys. *Journal of Materials Science*, **51(6)**, 3271–3276.

46. Guo, K., Qi, S., Wang, H., Huang, J., Wu, M., Yang, Y., et al. (2022) High-Voltage Electrolyte Chemistry for Lithium Batteries. *Small Science*, **2(5)**, 1–18.

47. Kim, D., Lim, J. M., Lim, Y. G., Park, M. S., Kim, Y. J., Cho, M., et al. (2015) Understanding of Surface Redox Behaviors of Li2MnO3 in Li-Ion Batteries: First-Principles Prediction and Experimental Validation. *ChemSusChem*, **8(19)**, 3255–3262.

48. Zhou, F., Cococcioni, M., Kang, K. and Ceder, G. (2004) The Li intercalation potential of LiMPO 4 and LiMSiO 4 olivines with M = Fe, Mn, Co, Ni. *Electrochemistry Communications*, **6(11)**, 1144–1148.

49. Ahniyaz, A., de Meatza, I., Kvasha, A., Garcia-Calvo, O., Ahmed, I., Sgroi, M. F., et al. (2021) Progress in solid-state high voltage lithium-ion battery electrolytes. *Advances in Applied Energy*, **4(September)**, 100070.

50. Li, A. -M., Wang, Z., Pollard, T. P., Zhang, W., Tan, S., Li, T., et al. (2024) High voltage electrolytes for lithium-ion batteries with micro-sized silicon anodes. *Nature Communications*, **15(1)**, 1–14.

51. Seo, D. H., Urban, A. and Ceder, G. (2015) Calibrating transition-metal energy levels and oxygen bands in first-principles calculations: Accurate prediction of redox potentials and charge transfer in lithium transition-metal oxides. *Physical Review B - Condensed Matter and Materials Physics*, **92(11)**, 1–11.

52. Wang, X., Sone, Y., Segami, G., Naito, H., Yamada, C. and Kibe, K. (2007) Understanding Volume Change in Lithium-Ion Cells during Charging and Discharging Using In Situ Measurements. *Journal of The Electrochemical Society*, **154(1)**, A14–A21.

53. Zhou, F., Cococcioni, M., Kang, K. and Ceder, G. (2004) The Li intercalation potential of LiMPO4 and LiMSiO4 olivines with M = Fe, Mn, Co, Ni. *Electrochemistry Communications*, **6(11)**, 1144–1148.

54. He, Q., Yu, B., Li, Z. and Zhao, Y. (2019) Density Functional Theory for Battery Materials. *Energy and Environmental Materials*, **2(4)**, 264–279.

55. Akgenc, B. (2019) Two-dimensional black arsenic for Li-ion battery applications: a DFT study. *Journal of Materials Science*, **54(13)**, 9543–9552.

56. Courtney, I. and Tse, J. (1998) Ab initio calculation of the lithium-tin voltage profile. *Physical Review B - Condensed Matter and Materials Physics*, **58(23)**, 15583–15588.

57. Joshi, R. P., Eickholt, J., Li, L., Fornari, M., Barone, V. and Peralta, J. E. (2019) Machine Learning the Voltage of Electrode Materials in Metal-Ion Batteries. *ACS Applied Materials and Interfaces*, **11(20)**, 18494–18503.

58. Islam, M. S., Driscoll, D. J., Fisher, C. A. J. and Slater, P. R. (2005) Atomic-scale investigation

of defects, dopants, and lithium transport in the LiFePO4 olivine-type battery material. *Chemistry of Materials*, **17(20)**, 5085–5092.

59. Huo, S., Sheng, L., Xue, W., Wang, L., Xu, H., Zhang, H., et al. (2023) Challenges of polymer electrolyte with wide electrochemical window for high energy solid-state lithium batteries. *InfoMat*, **5(3)**, 1–32.

60. He, X., Su, S., Zhang, B., Xiao, Z., Zhang, Z. and Ou, X. (2024) Alleviating the anisotropic microstructural change and boosting the lithium ions diffusion by grain orientation regulation for Ni-rich cathode materials. *Journal of Energy Chemistry*, **88**, 213–222.

61. Sazman, F. N., Zaki, N. H. M., Badrudin, F. W., Samat, M. H., Malik, N. A., Nor, N. A. N. M., et al. (2023) First-principles approach to the structural, electronic and intercalation voltage of Prussian blue (KxFe[Fe(CN)6]) (x = 1, 2) as potential cathode material for potassium ion batteries. *Journal of Solid State Electrochemistry*, **27(5)**, 1095–1106.

62. Xiong, Z. C., Xie, Y., Yi, T. F., Yu, H. T., Zhu, Y. R. and Zeng, Y. Y. (2014) Effect of lithium extraction on the stabilities, electrochemical properties, and bonding characteristics of LiFePO4 cathode materials: A first-principles investigation. *Ceramics International*, **40(2)**, 2655–2661.

63. Zhang, P., Zhang, D., Huang, L., Wei, Q., Lin, M. and Ren, X. (2012) First-principles study on the electronic structure of a LiFePO4 (010) surface adsorbed with carbon. *Journal of Alloys and Compounds*, **540(November)**, 121–126.

64. Zhou, F., Kang, K., Maxisch, T., Ceder, G. and Morgan, D. (2004) The electronic structure and band gap of LiFePO4 and LiMnPO 4. *Solid State Communications*, **132(3–4)**, 181–186.

65. Rosseinsky, D. R., Lim, H., Jiang, H. and Chai, J. W. (2003) Optical charge-transfer in iron(III)hexacyanoferrate(II): Electro-intercalated cations induce lattice-energy-dependent ground-state energies. *Inorganic Chemistry*, **42(19)**, 6015–6023.

66. Wojdeł, J. C. (2009) First principles calculations on the influence of water-filled cavities on the electronic structure of Prussian Blue. *Journal of Molecular Modeling*, **15(6)**, 567–572.